Processing and Application of Ceramics 19 [4] (2025) 322–333
https://doi.org/10.2298/PAC2504322C

$NiTiO_3$ ceramics prepared from mechanochemically synthesized powder: Structure, electrical and magnetic properties

Kumar P. Chandra[1], Anal K. Jha[2], Ajit R. Kulkarni[3], Kamal Prasad[4,*]

[1]*Department of Physics, S.M. College, Bhagalpur 812001, India*
[2]*University Department of Chemistry, T.M. Bhagalpur University, Bhagalpur 812007, India*
[3]*Department of Metallurgical Engineering and Materials Science, Indian Institute of Technology, Mumbai 400076, India*
[4]*University Department of Physics, T.M. Bhagalpur University, Bhagalpur 812007, India*

Received 1 August 2025; Received in revised form 9 November 2025; Accepted 23 November 2025

Abstract

Lead-free perovskite $NiTiO_3$ ceramic nanopowder was synthesized using the mixed-oxide method and high-energy ball milling, and finally uniaxially pressed and sintered at 1375 °C for 4 h. X-ray diffraction (XRD) confirmed a single-phase trigonal structure (space group $R\bar{3}$), with structural parameters refined using Rietveld analysis. The Williamson-Hall method was used to estimate lattice strain and crystallite size. To see if there exists any high-temperature phase in the system, high-temperature XRD up to 1000 °C was carried out, which indicated only an increase in lattice distortion leading to an increment in unit cell volume, and no change of the phase. The results indicated that dielectric constant remains almost temperature-insensitive up to 100 °C (temperature coefficient of capacitance, $T_{CC} \leq 5\%$) which shows its potential to be used for high temperature capacitor applications. Impedance spectroscopy and dielectric studies indicated non-Debye relaxation, with charge transport modelled by correlated barrier hopping theory. Morphological and compositional analyses verified sample purity. Magnetization studies revealed potential magneto-electric coupling. These properties suggest $NiTiO_3$ ceramics could be a promising candidate for high-density data storage and multifunctional applications.

Keywords: *lead-free perovskites, $NiTiO_3$ ceramics, mixed oxide method, electric and dielectric properties*

I. Introduction

Titanium-based oxides incorporating various metals, like $MTiO_3$ (M = Zn, Sr, Ni, Cu, Fe, Co), are well-established as multifunctional inorganic materials with broad applications across several fields. These include usage in solid oxide fuel cells electrodes [1], metal-air batteries [2], gas sensors [3], high-efficiency catalysts [4], chemical reactions [5] and electronics, due to their weak magnetism and semiconducting properties [6]. Among these, $NiTiO_3$ has emerged as a solid-lubricant, showing potential for lowering wear and friction in high temperature applications [7,8]. Also, it is known that for high-temperature ceramic capacitors and high-density data-storage systems, materials must combine thermal and chemical stability with a stable electrical and magnetic performance. Specifically, they should exhibit high dielectric constant, low dielectric loss, low temperature coefficient of capacitance over a working temperature range, ferroelectric (P_r) and magnetic (M_s) polarization, high coercive fields, stable insulation resistance over wide temperature ranges, low leakage currents, etc.

Previous research [9] has demonstrated that TiO_2 coatings containing Ni can effectively lubricate the surfaces without requiring liquid-lubricants. Significant efforts are being undertaken toward synthesizing $NiTiO_3$ powders and ceramics in pure form. $NiTiO_3$ is typically produced via conventional solid-state reaction method [6,10–13], as its characteristics are generally influenced by powder characteristics like purity, particle size and morphology. Cost-effective synthetic methods, such as co-precipitation [14,15], citrate [16], propionic acid [17]

*Corresponding author: +91 9934837317
e-mail: *k.prasad65@gmail.com*

and sol-gel techniques [14,18–24], have been widely explored for the preparation of $NiTiO_3$ nanocrystalline powders. Alternative synthesis approaches, such as combustion [25–27], molten salt [28], drop-quenching [29], polymeric precursor [30,31], hydrothermal [32], ultrasonic dispersion [33] and solvothermal methods [34], have also been investigated with the goal of enhancing different properties of the material.

To the best of our knowledge, no research has yet been reported on the formation of $NiTiO_3$ ceramic nanopowder via mechanochemical synthesis and studied this system at elevated temperatures. Considering the importance of the material, $NiTiO_3$ ceramic nanopowder was successfully prepared in the present study using an industrially viable mixed-oxide method. Fine powders with uniform particle size were obtained through high-energy ball milling. The as-prepared ceramic nanopowders were thoroughly characterized using X-ray diffraction (XRD), energy-dispersive X-ray spectroscopy (EDS), scanning electron microscopy (SEM), dielectric measurements, impedance spectroscopy, AC conductivity analysis and magnetic hysteresis studies. Besides, *in situ* high temperature XRD, dielectric and impedance studies of $NiTiO_3$ ceramics prepared from nanopowder have been undertaken with an aim of getting information about high temperature dielectric, impedance and AC conductivity behaviour which shall be able to further widen their intended applications window.

II. Experimental

2.1. Sample preparation

Polycrystalline $NiTiO_3$ powder was synthesized using analytical reagent (AR) grade chemicals (>99.9% pure, Merck), specifically $NiCO_3$ and TiO_2, via the mixed oxide synthesis method in an air atmosphere. The thermochemical reaction:

$$NiCO_3 + TiO_2 \xrightarrow{\Delta} NiTiO_3 + CO_2(g)\uparrow \qquad (1)$$

was carried out under the optimized calcination condition of 1350 °C for 5 h, employing controlled heating and cooling rates. This regimen ensured complete decomposition of the precursors, facilitated the formation of the desired perovskite phase, and minimized the emergence of a secondary phase or unreacted components. XRD analysis confirmed the reaction completion and formation of the $NiTiO_3$ phase. Thereafter, the calcined powder was subjected to extensive ball milling for 4 h to reduce particle size and enhance homogeneity. The milled powder was then pressed into a cylindrical pellet (10 mm diameter, 1.44 mm height) under a uniaxial pressure of 650 MPa. The pressed pellet was sintered at the optimized temperature of 1375 °C for 4 h in air atmosphere. This temperature-time combination was selected to promote effective densification and uniform grain development, while preventing the formation of secondary phases or abnormal grain growth. After sintering, the pellet exhibited a slight reduction in dimensions, with a final diameter of 9.92 mm and a thickness of 1.43 mm, corresponding to shrinkage of approximately 7%. The density of the resulting ceramics was measured to be greater than 91% of the theoretical density, indicating successful densification. Powder weight was monitored before and after sintering, showing a maximum difference of 1.96 mg out of 10 g, indicating minimal material loss and consistent composition. Consequently, the final sample composition was assumed to match the initial stoichiometry.

2.2. Structural characterization techniques

High temperature XRD data of the $NiTiO_3$ ceramics were recorded between 30 and 1000 °C using an X-ray diffractometer (XPERT-PRO, Pan Analytical) with CuKα radiation (λ = 1.5405 Å), scanning a Bragg angle range of $20° \leq 2\theta \leq 90°$ at a rate of 5.08 °/min. The room temperature *XY* (2θ vs. intensity) data were processed in WinPLOTR to determine peak positions, while unit cell parameters, *hkl* values and the space group of $NiTiO_3$ were extracted using DICVOL in the FullProf 2017 suite, with further refinement performed via FullProf's profile matching routine. Bragg peaks were fitted to the pseudo-Voigt function, with the background estimated through linear interpolation. The 3D visualization of the crystal structure of $NiTiO_3$ was performed by VESTA software. The Williamson-Hall approach was employed to calculate the crystallite size (D) and lattice strain from XRD peak broadening:

$$\eta \cos\theta = \frac{K\lambda}{D} + 2\frac{\Delta\xi}{\xi}\sin\theta \qquad (2)$$

Here η, K, $\Delta\xi/\xi$ and $K\lambda/D$ are XRD peak width at half intensity, lattice strain, Scherrer constant (0.89) and Scherrer particle size distribution, respectively. SEM micrograph of the calcined $NiTiO_3$ ceramic nanopowder was obtained by Nova NanoSEM NPEP303. The microstructure and EDAX analyses of the sintered $NiTiO_3$ sample were conducted on the fractured surface with a computer-controlled scanning electron microscope (SEM, Hitachi S-3400N, Japan). SEM image analysis was performed using OLYSIA m3 software.

2.3. Electric and magnetic properties measurement

The measurement of electrical impedance (Z) and phase angle (θ) was conducted over a frequency range of 1 Hz to 1 MHz and a temperature range of 50 to 900 °C using a Solartron SI1260 impedance/gain-phase analyser. The analysis was performed on a symmetric Ag|$NiTiO_3$|Ag cell during a cooling cycle, with conductive Ag paint applied on both faces of the pellet; the temperature was decreased at a rate of 1 °C/min. From the impedance data, the real and imaginary permittivity values were determined using standard equations:

$$\varepsilon'(\omega) = \frac{Z''}{\omega C_0 |Z|^2} \qquad (3)$$

$$\varepsilon''(\omega) = \frac{Z'}{\omega C_0 |Z|^2} \quad (4)$$

here $|Z| = [(Z')^2 + (Z'')^2]^{1/2}$. The real and imaginary components of the electric modulus and AC conductivity data were derived from the impedance data using standard equations:

$$M^*(\omega) = M'(\omega) + iM''(\omega) = \frac{\varepsilon'(\omega)}{|\varepsilon^*(\omega)|^2} + i\frac{\varepsilon''(\omega)}{|\varepsilon^*(\omega)|^2} \quad (5)$$

$$\sigma_{AC} = \omega \varepsilon_0 \varepsilon''(\omega) \quad (6)$$

Field-dependent magnetic properties of the test sample at room temperature were obtained using a vibrating sample magnetometer (Model 7410, Lake Shore Cryotronics, Inc.).

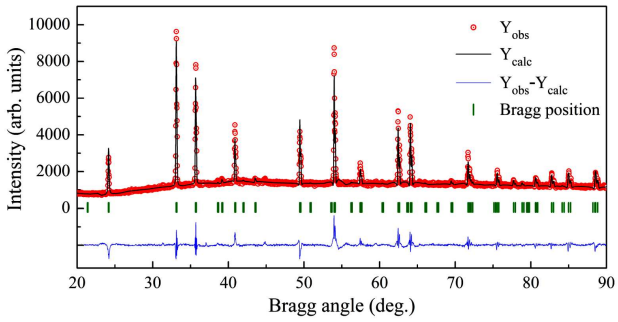

Figure 1. Rietveld refined pattern of sintered $NiTiO_3$ in the space group $R\bar{3}$ (symbols represent the observed data points and the solid lines their Rietveld fit)

Table 1. The crystal data and refinement factors of the sintered $NiTiO_3$ obtained from XRD data

Parameters	Results
Crystal system	Trigonal
Space group	$R\bar{3}$ (148)
a [Å]	5.0303
b [Å]	5.0303
c [Å]	13.7941
α [°]	90.000
β [°]	90.000
γ [°]	120.000
V [Å^3]	302.279
D_x [g/cm^3]	5.095
R_p	65.1
R_{wp}	30.7
R_{exp}	13.3
R_B	14.4
R_F	18.3
χ^2	5.329
d	0.6044
Q_D	2.61
S	2.3

III. Results and discussion

3.1. Structural analysis

The room-temperature XRD data for the sintered $NiTiO_3$ ceramic sample were refined using the Rietveld method, with space group $R\bar{3}$ (No. 148). As shown in Fig. 1, the final cycle of refinement produced closely matched observed and calculated profiles, with a χ^2 value of 5.329, indicating a reliable fit. The refinement was based on minimizing the χ^2 function, and XRD analysis confirmed that the sintered $NiTiO_3$ sample has a trigonal unit cell (consistent with JCPDS file number 33-0960). Table 1 summarizes the resulting crystal data and refinement factors.

Figure 2 presents the Williamson-Hall plot for the as-sintered $NiTiO_3$, with linear least-squares fitting of $\eta \cos\theta$-$\sin\theta$ data yielding an average crystallite size of 71 nm and a lattice strain of 0.0016. The minimal lattice strain is likely due to the thermochemical synthesis, which imposes fewer structural constraints compared to methods like extensive ball milling or strained layer growth [35]. The trigonal unit cell of the as-sintered $NiTiO_3$, as depicted in inset of Fig. 2, features alternating layers of Ni and Ti atoms oriented perpendicular to the c-axis. Oxygen atoms, positioned between the transition metal layers, are arranged in an octahedral coordination geometry surrounding the central Ni or Ti atoms. The atomic coordinates, along with their respective site multiplicities and Wyckoff notations, for the $NiTiO_3$ ceramics prepared from the nanopowder are provided in Table 2. Furthermore, Fig. 3 illustrates the temperature dependent XRD profiles of the $NiTiO_3$ ceramics be-

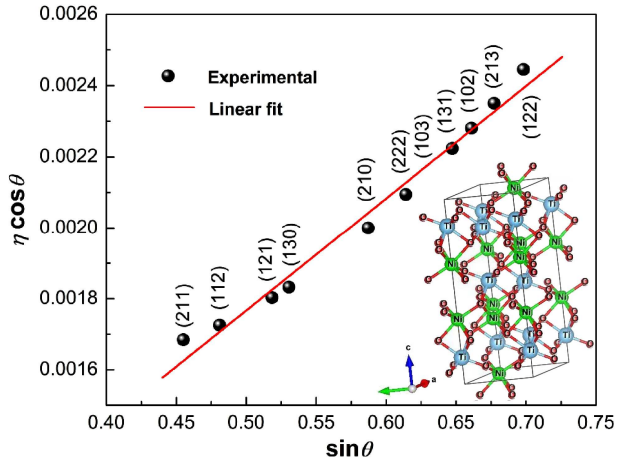

Figure 2. The Williamson-Hall plot of sintered $NiTiO_3$ sample (inset is unit cell of $NiTiO_3$)

Table 2. Coordinates of atoms and their sites (multiplicity and Wyckoff letter) of the sintered $NiTiO_3$ unit cell

Atom	Coordinates of atoms			Site
	x	y	z	
Ni	0.00000	0.00000	0.35070	6c
Ti	0.00000	0.00000	0.14450	6c
O	0.31600	0.01490	0.24710	18f

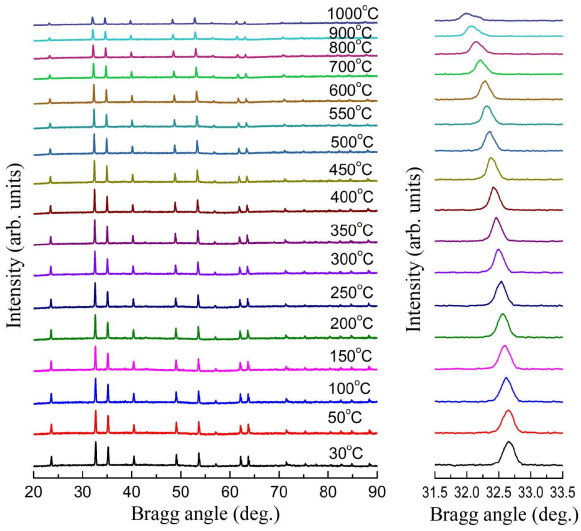

Figure 3. Temperature dependent XRD profiles of $NiTiO_3$ ceramics between 30 °C to 1000 °C and magnified XRD peak between 31.5°–33.5°

tween 30 and 1000 °C. It is observed that upon temperature rising there is a slight shift in the peak positions towards lower angle side (left) and change in intensities of the peaks, which could clearly be seen in the magnified region of the major peaks between 31.5°–33.5° (Fig. 3). The shift in diffraction peaks towards lower Bragg's angles with increasing temperature indicated the increase in lattice distortion leading to the increment in unit cell volume having no indication of phase change in the investigated temperature region.

Figure 4a presents SEM image of the calcined $NiTiO_3$ ceramic nanopowder, where the particles exhibit an approximately spherical morphology, with sizes ranging from 47 to 124 nm. The inset of Fig. 4b displays the SEM micrograph of the sintered $NiTiO_3$ ceramic sample, in which grains of varying sizes (11.3–20.1 μm) are dispersed throughout, indicating a polycrystalline microstructure. The average grain size in the sintered sample is estimated to be 16.2 ± 0.3 μm. Additionally, Fig. 4b shows the EDAX spectrum, where all peaks are attributed to the constituent elements of $NiTiO_3$, confirming its purity. The ratio of the average crystallite size to the grain size for sintered $NiTiO_3$ is approximately on the order of 10^{-2}.

3.2. Analysis of dielectric properties

The variations in frequency dependence of the real part (ε'), the imaginary part (ε'') and the loss tangent ($\tan\delta = \varepsilon''/\varepsilon'$) of the dielectric constant at different temperatures are depicted in Figs. 5a, 5b, 5c, respectively. Observations reveal that all parameters (ε', ε'' and $\tan\delta$) demonstrate an inverse relationship with frequency. A marked dispersion, coupled with a relatively high dielectric constant, is apparent in the ε'-f curve at lower frequencies, decreasing significantly at higher frequencies. This elevated dielectric constant at low frequencies is typical for dielectric materials and may stem from space charge contributions. At very low frequencies, the dipoles align with the applied field, resulting in ε' approaching ε_s (the dielectric constant under quasi-static conditions). As frequency rises, dipoles start to lag behind the field, causing a minor decline in ε', and a continuous drop of dielectric constant with frequency is noticed. At extreme frequencies, dipoles can no longer keep up with the field, and ε' approaches ε_∞.

3.3. Impedance spectroscopy analysis

Temperature dependences of ε' and $\tan\delta$ at several frequencies for the prepared $NiTiO_3$ sample are shown in Figs. 6a and 6b, respectively. Both ε' and $\tan\delta$ increase with the rise in temperature. Additionally, the $\tan\delta$-T plot shows a hump-like peak at each frequency, shifting towards higher temperatures with increase in frequency. Furthermore, the temperature coefficient of capacitance (T_{CC}), an essential parameter indicating low-temperature capacitance stability, is defined as:

$$T_{CC} = \frac{C_T - C_{RT}}{C_{RT}} \times 100 \qquad (7)$$

The obtained results indicate that ε' remains largely temperature-insensitive up to 100 °C ($T_{CC} \leq 5\%$) which shows its potential to be used for high temperature capacitor applications. At room temperature, ε' and ε'' are found to be 17.1 and 3.4, respectively, at 1 kHz.

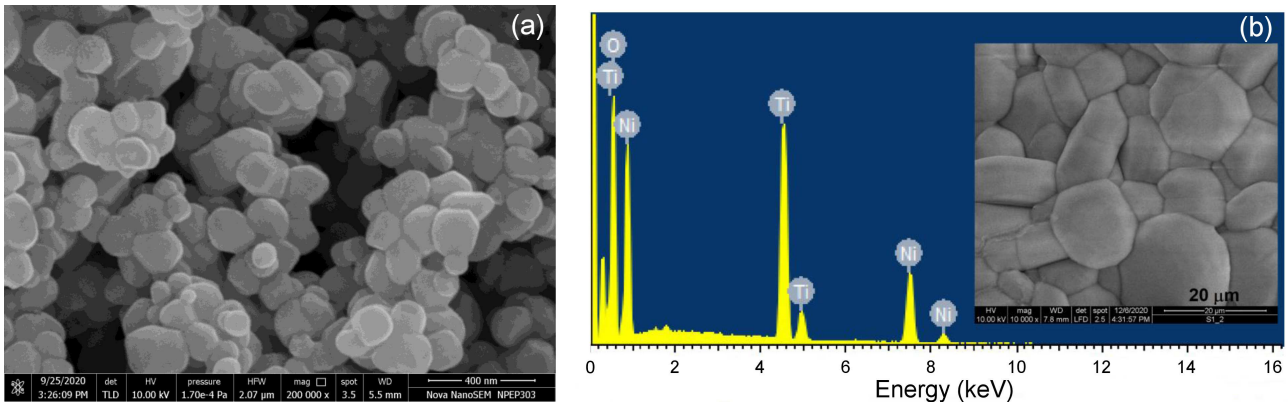

Figure 4. SEM image of calcined $NiTiO_3$ ceramic nanopowder (a) and EDAX spectrum and SEM micrograph (inset) of the sintered $NiTiO_3$ ceramics prepared from nanopowder (b)

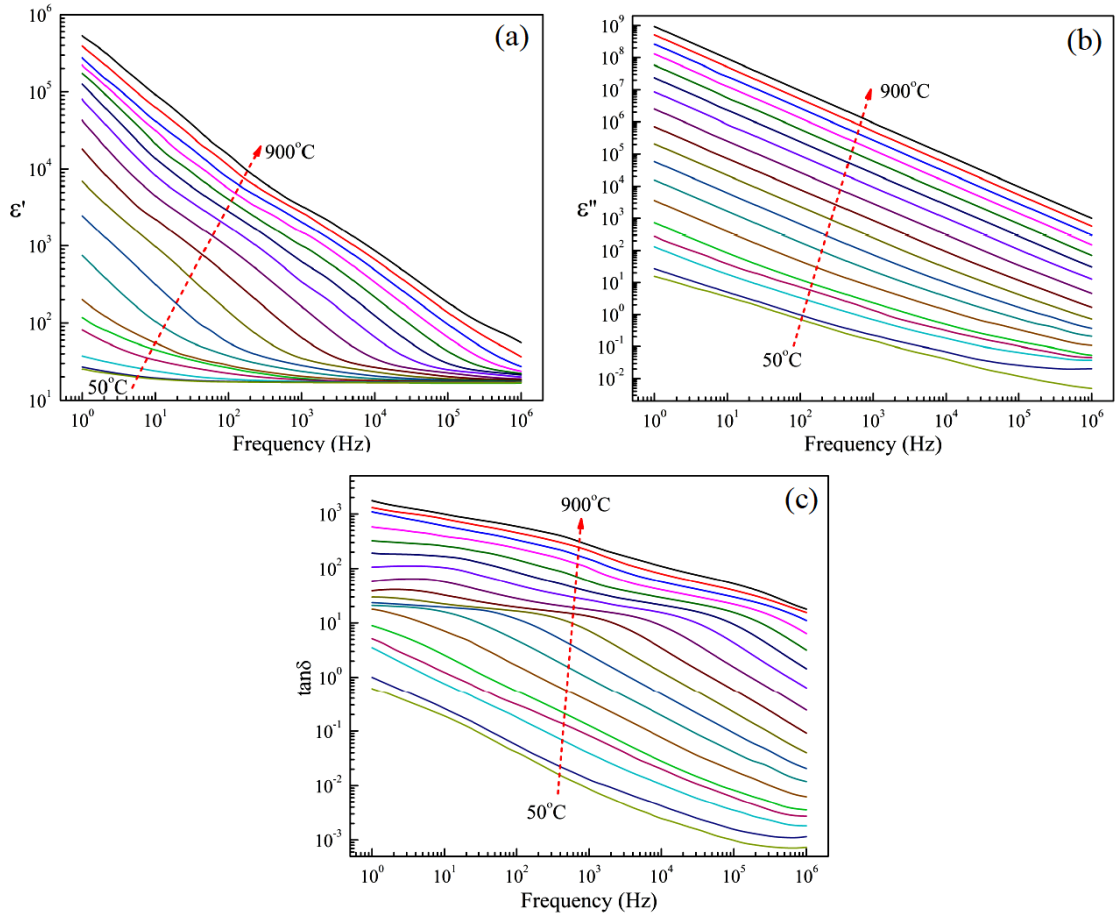

Figure 5. Variation of real (a) and imaginary (b) parts of dielectric constant and tangent loss (c) with frequency at different temperatures for $NiTiO_3$ ceramics prepared from nanopowder

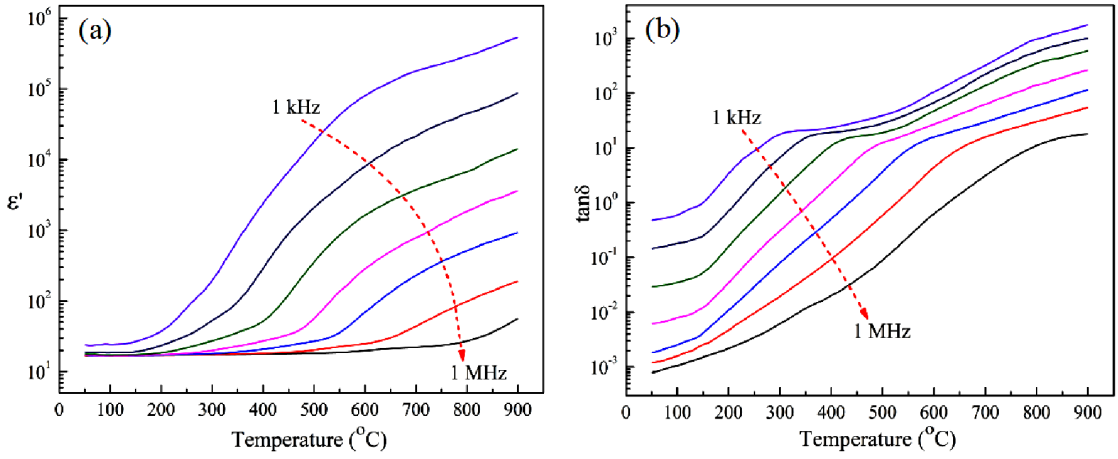

Figure 6. Variation of (a) real part of dielectric constant and (b) tangent loss with temperature at different frequencies for $NiTiO_3$ ceramics

Frequency dependences of the real (Z') and imaginary (Z'') components of impedance for the prepared $NiTiO_3$ sample at various temperatures are shown in Figs. 7a and 7b, respectively. As frequency increases, a consistent decline in magnitude of Z' is observed across all temperatures. Notably, the loss spectrum (Z''-f plots) exhibits significant features, including the appearance of asymmetric peaks (Z''_{max}), which decrease in magnitude and shift towards higher frequencies with temperature rising. The asymmetric broadening in the Z''-f plots suggests a distribution of relaxation times, implying a temperature-dependent electrical relaxation process in the material [36].

Figure 8 presents impedance data over a 1 Hz–1 MHz frequency range, displayed as a complex impedance spectra. As the temperature increases, curves bend towards the x-axis, indicating enhanced electrical conductivity. The complex plane plots exhibit a depressed,

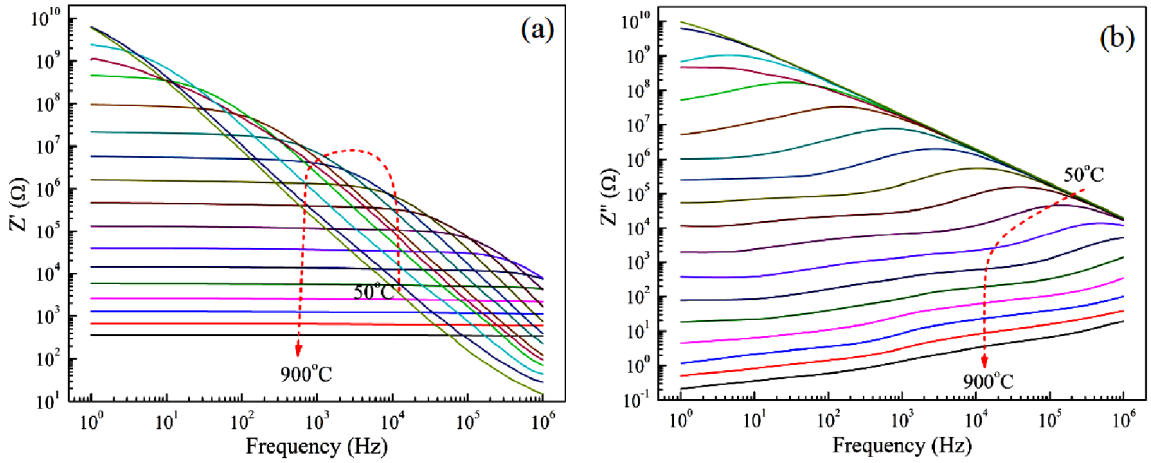

Figure 7. Variation of real (a) and imaginary (b) parts of impedance with frequency at different temperatures for $NiTiO_3$ ceramics

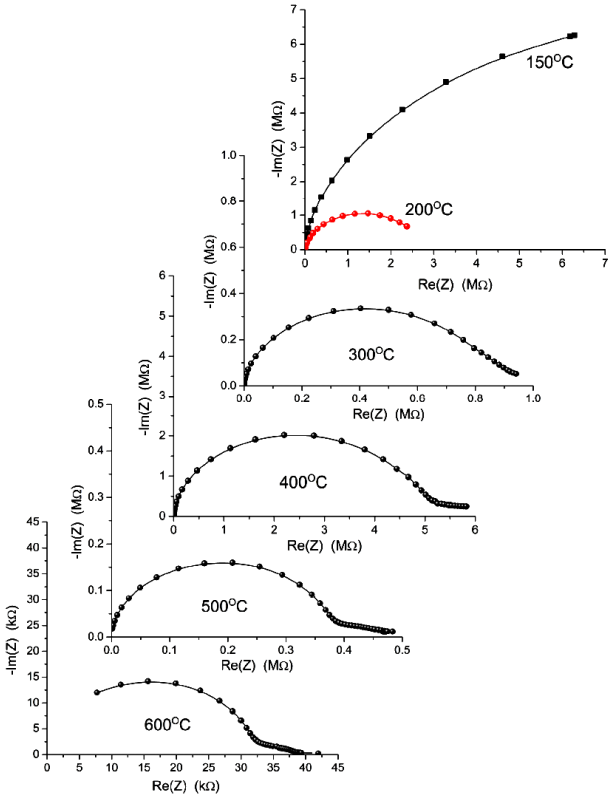

Figure 8. Cole-Cole plots at different temperatures for $NiTiO_3$ ceramics

asymmetric semicircular arc, with data shifting to higher values, suggesting the influence of grain boundaries. For Debye relaxation, semicircular plots are expected with centres on the real axis. In contrast, the observed non-Debye relaxation manifests as semicircular arcs with endpoints on the real axis and centres below it. This behaviour is described by the complex impedance expression:

$$Z^*(\omega) = Z' + iZ'' = \frac{R}{1 + (i\frac{\omega}{\omega_0})^{1-\alpha}} \qquad (8)$$

where α quantifies the deviation from ideal Debye relaxation. When α approaches zero, Eq. 8 aligns with the Debye's model. The impedance plots show non-ideal semicircles, with centres below the x-axis, indicating $\alpha > 0$, increasing with temperature and suggesting non-Debye relaxation in $NiTiO_3$, consistent with prior studies [36–39]. This may result from distributed elements within the material-electrode interface.

The dielectric response can also be analysed through the electric modulus, $M^*(\omega) = 1/\varepsilon^*(\omega)$, a reciprocal quantity that minimizes artefacts from electrode polarization. Key features of $M^*(\omega)$ include a broad, asymmetric peak in its imaginary part and a sigmoidal step in the real part. These patterns resemble the response seen in the loss and storage of mechanical stress during relaxation processes, allowing for similar interpretations. Frequency dependences of the real (M') and imaginary (M'') components of the electric modulus at various temperatures are shown in Figs. 9a and 9b, respectively. The real part, M', exhibits very low values at low frequencies, followed by a sigmoidal increase as frequency rises, eventually reaching M_∞. This behaviour likely result from conduction associated with the short-range mobility of charge carriers. The imaginary part, M'', exhibits distinct frequency-dependent characteristics, including: i) peaks at unique frequencies across different temperatures, ii) pronounced peak asymmetry, with positions in the dispersion region of the M''-f plot and iii) peak shifts towards higher frequencies as temperature increases. The low-frequency side of the M'' peak reflects the frequency range where charge carriers experience long-range mobility, allowing them to hop between neighbouring sites. Conversely, the high-frequency side corresponds to frequencies where carriers are confined within potential wells, limited to localized movement. Thus, the peak position in M'' suggests a transition from long-range to short-range mobility as frequency rises [37] while the peak in the modulus spectrum provides a clear indication of conductivity relaxation. Additionally, the M'' peaks broaden with increasing temperature,

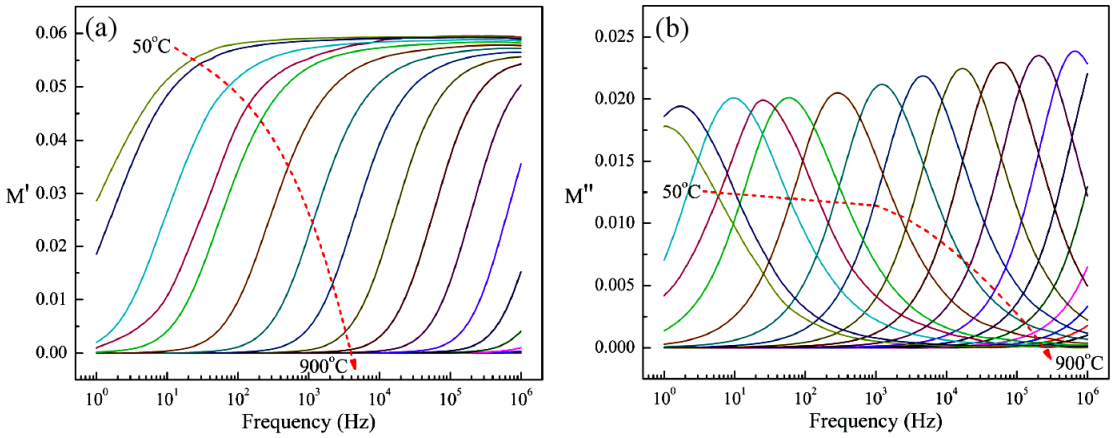

Figure 9. Variation of real (a) and imaginary (b) parts of electric modulus with frequency at different temperatures for $NiTiO_3$ ceramics

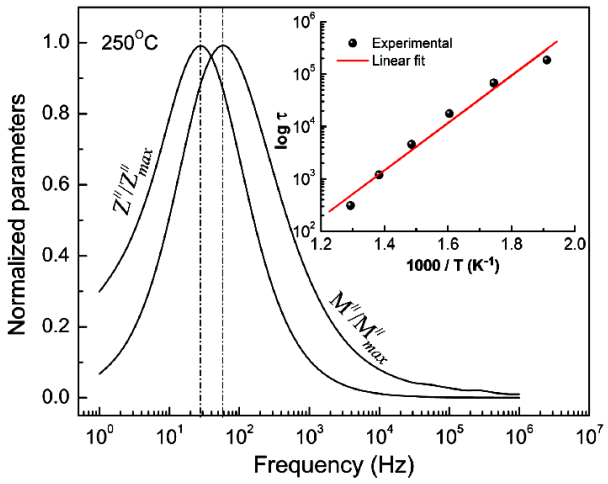

Figure 10. Variation of normalized Z'' and M'' with frequency at 250 °C for $NiTiO_3$ ceramics (inset: temperature dependence of the relaxation time)

indicating enhanced non-Debye behaviour - a unique trait of electrical relaxation, as most other relaxation processes (e.g. mechanical or light scattering) tend to approach Debye-like behaviour with temperatures rising [38].

The relaxation times, defined as $\tau = 1/\omega_m$, were calculated from the peak frequency (f_m) at M''_{max} (Fig. 9b), where relaxation occurs at $\omega_m \cdot \tau = 1$. The temperature dependence of τ adheres to the Arrhenius relation:

$$\tau = \tau_0 \exp\left(-\frac{U}{k_B T}\right) \tag{9}$$

where τ_0 is the pre-exponential factor and U is the activation energy. The inset of Fig. 10 presents a plot of $\log \tau$ versus $10^3/T$, yielding values of $\tau_0 = 2.798 \times 10^{-15}$ s and $U = 0.447$ eV via linear least squares fitting. The small τ_0 suggests that the dielectric relaxation in $NiTiO_3$ likely involves small polaron dynamics, with τ_0 for typical lattice dipole relaxation near 10^{-14} s [38]. In order to illustrate that the peaks of the scaled parameters (Z''/Z''_{max} and M''/M''_{max}) are not occurring at the same frequency, their variation at 250 °C (as an example) have been plotted in Fig. 10 for the $NiTiO_3$ ceramics. The peaks of these parameters do not align; instead, they follow a sequence: $f_{Z''} < f_{M'}$ indicating different peak frequencies. This peak mismatch, which increases with temperature, suggests changes in polarization behaviour. While peak overlap signifies long-range conductivity, their divergence implies short-range conductivity, potentially facilitated by a hopping mechanism [37,40,41].

Figure 11 presents the scaled plots of $Z''(\omega, T)$ and $M''(\omega, T)$ versus reduced frequency, with f_{max} marking the peak frequency in the Z''- or M''-frequency plots. Both Z''- and M''-data merge into a single, master curve, and the full width at half maximum (FWHM) exceeds 1.14 decades. These results suggest that the relaxation times' distribution function is almost temperature-independent, indicating a non-exponential, non-Debye relaxation process. This phenomenon follows the relationship:

$$\phi(t) = \exp\left[-\left(\frac{t}{\tau}\right)^{\beta}\right]; \ (0 < \beta < 1) \tag{10}$$

that is associated to $M^*(\omega)$ as:

$$M^*(\omega) = \frac{1}{\varepsilon_\infty}\left(1 - L\left(-\frac{\mathrm{d}\phi}{\mathrm{d}t}\right)\right) \tag{11}$$

where β ($= 1/W$) is the Kohlrausch exponent, $L(x)$ denotes the Laplace transform of x, and W is the FWHM. A lower β value implies greater deviation from Debye-type relaxation ($\beta = 1$). Such non-exponential relaxation suggests ion migration via hopping and the correlated mobility of nearby charge carriers [29]. This superposition of data across frequencies points to a similar thermal activation energy (~0.5 eV) for all dynamic processes, indicating the presence of a single type of charge carrier. Thus, both peaks in Fig. 11 likely represent the same underlying relaxation process. The results further suggest that the observed dielectric relaxation in $NiTiO_3$ arises predominantly from bulk effects [39].

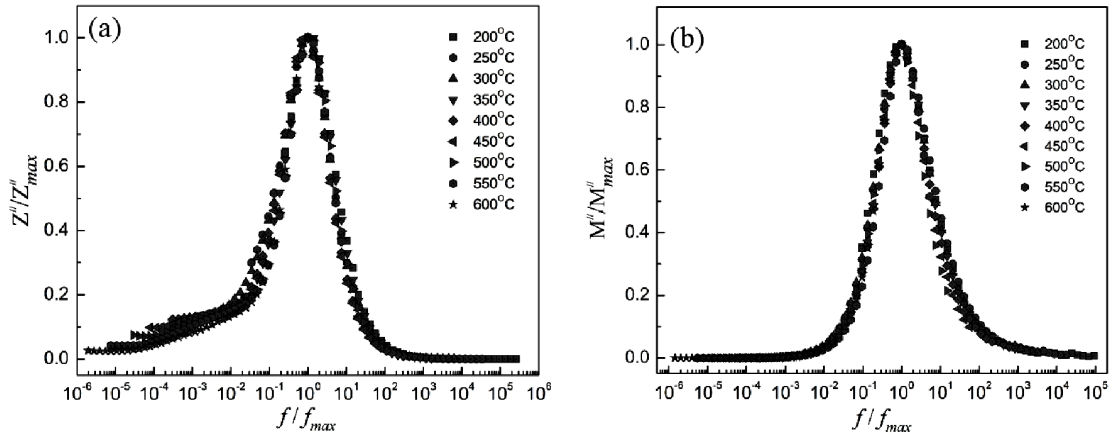

Figure 11. Scaling behaviour of Z'' (a) and M'' (b) for $NiTiO_3$ ceramics

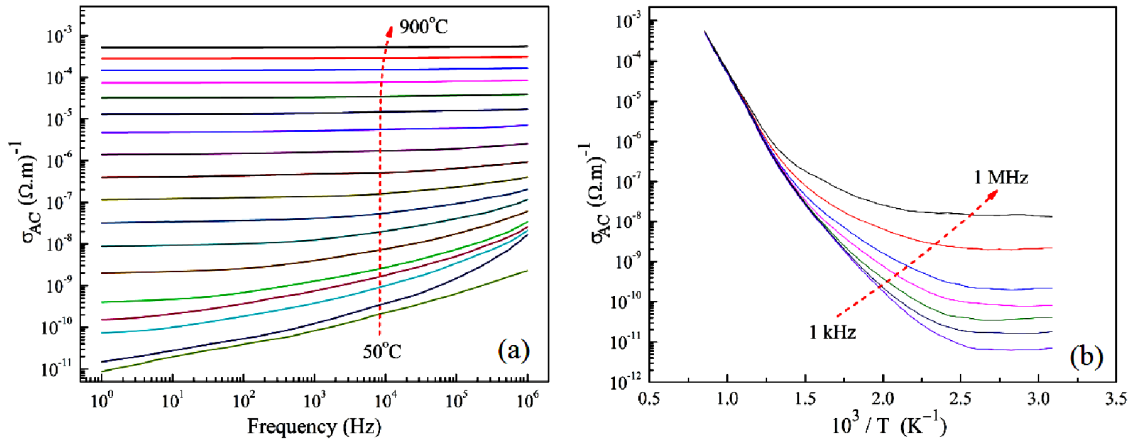

Figure 12. Variation of AC conductivity with frequency at different temperatures (a) and with inverse of temperature at different frequencies (b) for $NiTiO_3$ ceramics

Figure 12a illustrates the frequency-dependent AC electrical conductivity (σ_{AC}) of the prepared $NiTiO_3$ ceramics measured across varying temperatures. The conductivity plots exhibit dispersion throughout the studied frequency range, with higher temperatures leading to a plateau-like behaviour indicative of reduced frequency dependence. The transition from frequency-independent to frequency-dependent regions signifies the onset of conductivity relaxation, highlighting a shift from long-range hopping to localized ion motion. This behaviour aligns with the hopping conduction mechanism, which is characteristic of materials possessing a high density of localized states within a semiconductor-like bandgap. Additionally, the formation of polarons due to the charge carrier localization facilitates nearest-neighbour hopping conduction [42,43]. Figure 12b displays the temperature dependence of σ_{AC} at different frequencies. The activation energy (E_a) for conduction was determined using the Arrhenius relationship:

$$\sigma_{AC} = \sigma_0 \exp\left(-\frac{E_a}{k_B T}\right) \tag{12}$$

Linear fitting of the data to this equation yielded apparent activation energies of 0.97 eV and 0.47 eV for frequencies of 1 kHz and 1 MHz, respectively. The lower activation energy suggests carrier transport via hopping between localized states in a disordered matrix [44,45]. The enhanced electrical conductivity observed in the $NiTiO_3$ ceramics can be attributed to oxygen vacancies introduced during the sintering process: $O_O \rightarrow \frac{1}{2} O_2 \uparrow + V_O^{\bullet\bullet} + 2e^-$, which increase conductivity, dielectric loss, and space charge accumulation at grain boundaries, potentially impacting material performance [46]. Further, the σ_{AC} in materials with localized states is typically expressed as:

$$\sigma_{AC} = \sigma_0 + A\omega^s \tag{13}$$

Here, σ_0 represents the frequency-independent (DC or electronic) component of conductivity, s ($0 \leq s \leq 1$) is the frequency exponent, ω is the angular frequency of the applied AC field and $A = \pi N^2 e^2 / 6 k_B T (2\alpha)$ is a constant. In this expression, e, T, k_B, α and N are the electronic charge, absolute temperature, Boltzmann's constant, polarizability of a site pair, and density of hopping sites per unit volume respectively. This behaviour arises from the movement of charge carriers, which hop over a characteristic length R_H between localized sites distributed randomly within the material. The term $A\omega^s$

can be interpreted through two principal mechanisms of charge carrier transport: i) quantum mechanical tunnelling (QMT) across the barriers separating localized sites and ii) correlated barrier hopping (CBH), where carriers overcome these barriers. Both models predict distinct temperature- and frequency-dependent trends in the exponent s, reflecting the underlying conduction processes. According to QMT model, s remains unaffected by temperature and decreases with increasing ω. In contrast, in CBH model, σ_{AC} is described as [47,48]:

$$\sigma_{AC} = \frac{\pi}{3} e^2 \omega k_B T [N(E_f)]^2 \alpha^{-5} \left[\ln \frac{f_0}{\omega} \right]^4 \quad (14)$$

Here, $N(E_f)$, f_0 and α are the density of states at Fermi level, photon frequency and localized wave function respectively. The frequency exponent s and minimum hopping distance, R_{min} are further expressed as [49]:

$$s = 1 - \frac{6k_B T}{W_m} \quad (15)$$

$$R_{min} = \frac{2e^2}{\pi \varepsilon \varepsilon_0 W_m} \quad (16)$$

In this context, W_m refers to the binding energy, defined as the energy required to transfer an electron completely from one site to another. The parameters ε and ε_0 represent the dielectric constants of $NiTiO_3$ and vacuum, respectively.

Using Eq. 14, the values of $N(E_f)$ were determined with the assumptions $f_0 = 10^{13}$ Hz and $\alpha = 10^{10}\,m^{-1}$, across a range of frequencies and temperatures. Figure 13 depicts the frequency-dependent variation of $N(E_f)$ at different temperatures. The results show that $N(E_f)$ decreases with increasing frequency and converges at frequencies above 100 kHz. The inset of Fig. 13 highlights the temperature dependence of $N(E_f)$ at different frequencies, revealing that $N(E_f)$ consistently increases with temperature across all frequencies. At lower frequencies, electrical conduction is influenced by both frequency and temperature, whereas at higher frequencies, the localized charge carriers are primarily affected by thermal excitation. These findings align with the trends observed in the dielectric loss (Fig. 6b) and AC conductivity (Fig. 12b). The elevated $N(E_f)$ values indicate a dominant hopping mechanism of charge transport between pairs of sites in $NiTiO_3$ [42,50,51].

The minimum hopping length, R_{min}, was derived from Eq. 16. Figure 14 illustrates the frequency dependence of R_{min} at various temperatures. At low frequencies, R_{min} exhibits small values ($\sim 10^{-11}$ m) and displays dispersion with increasing frequency, eventually saturating at an asymptotic maximum in the high-frequency region. This behaviour suggests the absence of a restoring force governing charge carrier mobility under an applied electric field, consistent with long-range charge carrier mobility. Additionally, the sigmoidal rise in R_{min} with frequency, leading to the saturation, suggests short-range charge carrier mobility at higher frequencies [50,51]. The inset of Fig. 14 presents the temperature dependence of R_{min} at various frequencies, where R_{min} decreases with temperature at lower frequencies, reaching a maximum before stabilizing, supporting the above observations. Notably, R_{min} is approximately four orders of magnitude smaller than the grain size of $NiTiO_3$.

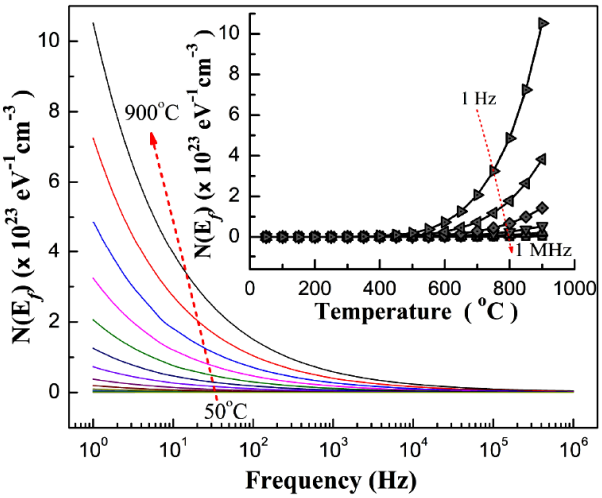

Figure 13. Variation of $N(E_f)$ with frequency at different temperatures for $NiTiO_3$ ceramics (inset: temperature dependence of $N(E_f)$ at different frequencies)

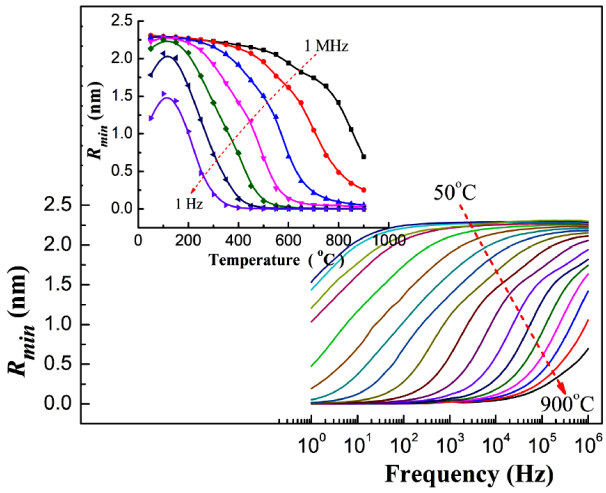

Figure 14. Variation of R_{min} with frequency at different temperatures for $NiTiO_3$ ceramics (inset: temperature dependence of R_{min} at different frequencies)

The magnetization (M) versus applied magnetic field (H) curve for the synthesized $NiTiO_3$ ceramic nanopowder, recorded at room temperature, is presented in Fig. 15. The M-H plot reveals characteristic ferromagnetic behaviour, indicative of super-exchange interactions occurring between Ni^{2+} ions mediated via oxygen atoms [52,53]. The magnetic interactions are primarily attributed to Ni^{2+} ions, which possess a $3d^8$ electronic configuration with partially filled $3d$ orbitals $(t_{2g})^6(e_g)^2$, conducive to inducing magnetic properties. In contrast,

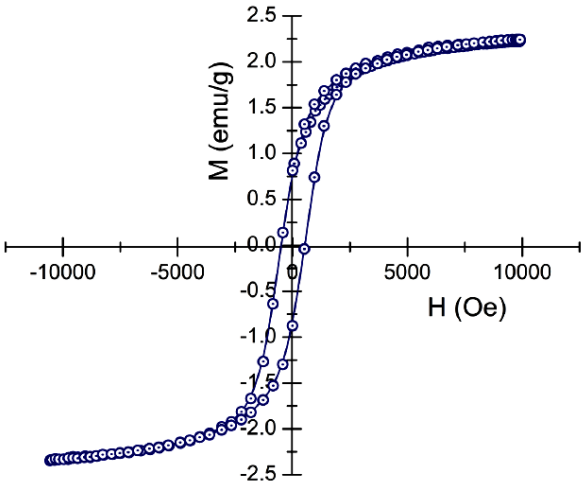

Figure 15. Magnetization curve at room temperature for $NiTiO_3$ ceramics

Ti^{4+} ions exhibit a $3d^0$ configuration, indicative of diamagnetic behaviour. Additionally, the empty $3d^0$ orbitals of Ti^{4+} ions contribute to polar behaviour, which is favourable for inducing ferroelectricity in $NiTiO_3$ [54]. The coercive field (H_c), remanent magnetization (M_r), and saturation magnetization (M_s) were determined to be 520.78 Oe, 0.81 emu/g and 2.042 emu/g, respectively. The low H_c value suggests potential applicability in magnetic recording devices. These findings indicate the possibility of magnetoelectric coupling in the material, suggesting that electric ordering at the microscopic scale may influence magnetic properties.

IV. Conclusions

Polycrystalline $NiTiO_3$ ceramics, obtained from nanopowder synthesized via a high-temperature solid-state reaction followed by extensive ball milling, exhibits a perovskite-like trigonal structure within the $R\bar{3}$ (No. 148) space group. Temperature dependent X-ray diffraction study suggested the increase in unit cell volume without the phase change in the system up to 1000 °C. Dielectric analysis demonstrated the material's suitability for high-temperature capacitor applications and exhibited non-Debye relaxation behaviour, with AC conductivity adhering to the universal power law. Charge transport mechanisms were effectively explained by the pair approximation-based correlated barrier hopping model, with the minimum hopping length calculated to be approximately 10^{-4} times smaller than the grain size. Magnetoelectric coupling was examined using vibrating sample magnetometry, highlighting the multifunctional potential of this system. These findings suggest that the synthesized ceramic nanopowder possesses multifunctional properties, making it a promising candidate for high-density data storage technologies.

Acknowledgement: Authors acknowledge Central Instrumentation Facility (CIF) at Savitribai Phule Pune University, Pune for providing the SEM image

References

1. O. Yamamoto, Y. Takeda, R. Kanno, M. Noda, "Perovskite-type oxides as oxygen electrodes for high temperature oxide fuel cells", *Solid State Ionics*, **22** [2-3] (1987) 241–246.
2. Y. Shimizu, K. Uemura, N. Miura, N Yamazoe, "Gas-diffusion electrodes for oxygen reduction loaded with large surface area $La_{1-x}Ca_xMO_3$ (M = Co, Mn)", *Chem. Lett.*, **17** [12] (1988) 1979–1982.
3. H. Obayashi, Y. Sakurai, T. Gejo, "Perovskite-type oxides as ethanol sensors", *J. Solid State Chem.*, **17** (1976) 299-303.
4. H. Tanaka, M. Misono, "Advances in designing perovskite catalysts", *Curr. Opin. Solid State Mater. Sci.*, **5** [5] (2001) 381–387.
5. M. Lerch, H. Boysen, R. Nerder, F. Frey, W. Laqua, "Neutron scattering investigation of the high temperature phase transition in $NiTiO_3$", *J. Phys. Chem. Solids*, **53** [9] (1992) 1153–1156.
6. R.S. Singh, T.H. Ansari, R.A. Singh, B.M. Wanklyn, "Electrical conduction in $NiTiO_3$ single crystals", *Mater. Chem. Phys.*, **40** [3] (1995) 173–177.
7. D.J. Taylor, P.F. Fleig, R.A. Page, "Characterization of nickel titanate synthesized by sol-gel processing", *Thin Solid Films*, **408** [1-2] (2002) 104–110.
8. D.J. Taylor, P.F. Fleig, S.T. Schwab, R.A. Page, "Sol-gel derived, nanostructured oxide lubricant coatings", *Surf. Coat. Technol.*, **120** (1999) 465–460.
9. R.A. Page, C.R. Blanchard-Ardid, W. Wei, "Effect of particulate additions on the contact damage resistance of hot-pressed Si_3N_4", *J. Mater. Sci.*, **23** (1988) 946–957.
10. A. Kale, S. Gubbala, R.D.K. Misra, "Magnetic behavior of nanocrystalline nickel ferrite synthesized by the reverse micelle technique", *J. Mag. Mag. Mater.*, **277** [3] (2004) 350–358.
11. J.A. Jiang, Q. Ga, Z. Chen, J. Hu, C. Wu, "Syntheses, characterization and properties of novel nanostructures consisting of Ni/titanate and Ni/titania", *Mater. Lett.*, **60** [29-30] (2006) 3803–3808.
12. Y.K. Sharma, M. Kharkwal, S. Uma, R. Nagarajan, "Synthesis and characterization of titanates of the formula $MTiO_3$ (M = Mn, Fe, Co, Ni and Cd) by co-precipitation of mixed metal oxalates", *Polyhedron*, **28** (2009) 579–585.
13. T. Li, C.C. Wang, C.M. Lei, X.H. Sun, G.J. Wang, L.N. Liu, "Conductivity relaxation in $NiTiO_3$ at high temperatures", *Curr. Appl. Phys.*, **13** [8] (2013) 1728–1731.
14. A.V. Murugan, V. Samuel, S.C. Navale, V. Ravi, "Phase evolution of $NiTiO_3$ prepared by coprecipitation method", *Mater. Lett.*, **60** [15] (2006) 1791–1792.
15. M.A. El-Fattah Gabal, Y.M.A. Angari, A.Y. Obaid, "Structural characterization and activation energy of $NiTiO_3$ nanopowders prepared by the co-precipitation and impregnation with calcinations", *Comptes Rendus Chimie*, **16** [3] (2013) 704–711.
16. H. Taguchi, D. Matsuda, M. Nagao, K. Tanihata, Y. Miyamoto, "Synthesis of perovskite-type $(La_{1-x}Sr_x)MnO_3$ ($O < x < 0.3$) at low temperature", *J. Am. Ceram. Soc.*, **75** [1] (1992) 201–202 .
17. T. Harikawa, N. Mikami, T. Markita, J. Tanimura, M. Kataoka, K.S.K. Sato, M.N.M. Nunoshita, "Dielectric properties of $(Ba,Sr)TiO_3$ thin films deposited by rf sputtering", *Jpn. J. Appl. Phys.*, **32** [95] (1993) 4126.
18. C. Pavithra, W. Madhuri, "Electrical and magnetic prop-

erties of $NiTiO_3$ nanoparticles synthesized by the sol-gel synthesis method and microwave sintering", *J. Mater. Res. Technol*., **8** [3] (2019) 3097–3101.
19. V. Chellasamy, P. Thangadurai, "Structural and electrochemical investigations of nanostructured $NiTiO_3$ in acidic environment", *Front. Mater. Sci*., **11** [2] (2017) 162–170.
20. S.M. Hosseinpour-Mashkani, M. Maddahfar, A. Sobhani-Nasab, "Novel silver-doped $NiTiO_3$: auto-combustion synthesis, characterization and photovoltaic measurements", *S. Afr. J. Chem*., **70** (2017) 44–48.
21. A. Sobhani-Nasab, S.M. Hosseinpour-Mashkani, M. Salavati-Niasari, H. Taqriri, S. Bagheri, K. Saberyan, "Synthesis, characterization, and photovoltaic application of $NiTiO_3$ nanostructures via two-step sol-gel method", *J. Mater. Sci. Mater. Electron*., **26** (2015) 5735–5742.
22. A.B. Gambhire, M.K. Lande, S.B. Kalokhe, A.B. Mandale, K.R. Patil, R.S. Gholap, B.R. Arbad, "Synthesis and characterizations of $NiTiO_3$ nanoparticles prepared by the sol-gel process", *Philos. Mag. Lett*., **88** [6] (2008) 467–472.
23. S.-H. Chuang, M.-L. Hsieh, D.-Y. Wang, "Structure and dielectric properties of $NiTiO_3$ powders synthesized by the modified sol-gel method", *J. Chin. Chem. Soc.,* **59** (2012) 628–632.
24. A.R. Phani, S. Santucci, "Structural characterization of nickel titanium oxide synthesized by sol-gel spin coating technique", *Thin Solid Films*, **396** [1-2] (2001) 1–4.
25. G.A. Traistaru, C.I. Covaliu, V. Matei, D. Cursaru, I. Jitaru, "Synthesis and characterization of $NiTiO_3$ and $NiFe_2O_4$ as catalysts for toluene oxidation", *Digest J. Nanomater. Biostruct*., **6** [3] (2011) 1257–1263.
26. Y. Tong, J. Fu, Z. Chen, "Synthesis, characterization, and NIR reflectance of highly dispersed $NiTiO_3$ and $NiTiO_3/TiO_2$ composite pigments", *J. Nanomater*., **2016** (2016) 5464978.
27. M.E.Z. Morín, L. Torres-Martínez, D. Sanchez-Martínez, C. Gómez-Solís, "Photocatalytic performance of titanates with formula $MTiO_3$ (M = Fe, Ni, and Co) synthesized by solvo-combustion method", *Mater. Res*., **20** [5] (2017) 1322–1331.
28. S. Yuvaraj, V.D. Nithya, K.S. Fathima, C. Sanjeeviraja, G.K. Selvan, S. Arumugam, R.K. Selvan, "Investigations on the temperature dependent electrical and magnetic properties of $NiTiO_3$ by molten salt synthesis", *Mater. Res. Bull*., **48** [3] (2013) 1110–1116.
29. S. Klemme, W. Hermes, M. Eul, C.H. Wijbrans, A. Rohrbach, R. Pöttgen, "New thermodynamic data for $CoTiO_3$, $NiTiO_3$ and $CoCO_3$ based on low-temperature calorimetric measurements", *Chem. Cent. J*., **5** (2011) 54.
30. K.P. Lopes, L.S. Cavalcante, A.Z. Simões, J.A. Varela, E. Longob, E.R. Leite, "$NiTiO_3$ powders obtained by polymeric precursor method: Synthesis and characterization", *J. Alloys Comp*., **468** [1-2] (2009) 327–332.
31. J.-L. Wang, Y.-Q. Li, Y.-J. Byon, S.-G. Mei, G.-L. Zhang, "Synthesis and characterization of $NiTiO_3$ yellow nano pigment with high solar radiation reflection efficiency", *Powder Technol*., **235** (2013) 303–306.
32. R. Hang, S. Liu, Y. Liu, Y. Zhao, L. Bai, M. Jin, X. Zhang, X. Huang, X. Yao, B. Tang, "Preparation, characterization, corrosion behavior and cytocompatibility of $NiTiO_3$ nanosheets hydrothermally synthesized on biomedical NiTi alloy", *Mater. Sci. Eng. C*, **97** (2019) 715–722.
33. S. Karmakar, A.K. Manna, S. Varma, D. Behera, "Investigation of optical, electrical and magnetic properties of hexagonal $NiTiO_3$ nanoparticles prepared via ultrasonic dispersion techniques for high power applications", *Mater. Res. Express,* **5** [5] (2018) 055037.
34. C.-H. Lu, N. Naresh, P.S. Kumar, S. Som, "Microwave-assisted solvothermal synthesis and electrochemical characterizations of ternary perovskite $NiTiO_3$ anode materials for lithium ion batteries", *Ceram. Int.,* **45** [15] (2019) 19517–19521.
35. U.K. Mahto, S.K. Roy, K. Prasad, "High energy milled $Ba_{0.06}Na_{0.47}Bi_{0.47}TiO_3$ ceramic: structural and electrical properties", *IEEE Transac. Dielectr. Elect. Insulat.,* **25** [1] (2018) 174-180.
36. K. Prasad, Lily, K. Kumari, K.P. Chandra, K.L. Yadav, S. Sen, "Electrical properties of a lead-free perovskite ceramic: $(Na_{0.5}Sb_{0.5})TiO_3$", *Appl. Phys. A*, **88** [2] (2007) 377–383.
37. M.A.L. Nobre, S. Lanfredi, "Dielectric spectroscopy on $Bi_3Zn_2Sb_3O_{14}$ ceramic: an approach based on the complex impedance", *J. Phys. Chem. Solids*, **64** [12] (2003) 2457–2464.
38. K. Prasad, K. Kumari, Lily, K.P. Chandra, K.L. Yadav, S. Sen, "Electrical conduction in $(Na_{0.5}Bi_{0.5})TiO_3$ ceramic: Impedance spectroscopy analysis", *Adv. Appl. Ceram.*, **106** [5] (2007) 241–246.
39. W.-H. Jung, J.-H. Lee, J.-H. Sohn, H.-D. Nam, S.-H. Cho, "Dielectric loss anomaly in $Ba(Fe_{1/2}Ta_{1/2})O_3$ ceramic", *Mater. Lett*., **56** [3] (2002) 334–338.
40. R. Gerhardt, "Impedance and dielectric spectroscopy revisited: Distinguishing localized relaxation from long-range conductivity", *J. Phys. Chem. Solids,* **55** [12] 1491-(1994) 1506.
41. W. Cao, R. Gerhardt, "Calculation of various relaxation times and conductivity for a single dielectric relaxation process", *Solids State Ionics*, **42** [3-4] (1990) 213-221.
42. S. Bhagat, K. Prasad, "Structural and impedance spectroscopy analysis of $Ba(Fe_{1/2}Nb_{1/2})O_3$ ceramic", *Phys. Status Solidi A*, **207** [5] (2010) 1232–1239.
43. K. Prasad, S. Bhagat, Priyanka, K. AmarNath, K.P. Chandra, A.R. Kulkarni, "Electrical properties of $BaY_{0.5}Nb_{0.5}O_3$ ceramic: Impedance spectroscopy analysis", *Physica B*, **405** [17] (2010) 3564–3571.
44. Lily, K. Kumari, K. Prasad, K.L. Yadav, "Dielectric and impedance study of lead-free ceramic: $(Na_{0.5}Bi_{0.5})ZrO_3$", *J. Mater. Sci.*, **42** [15] (2007) 6252–6259.
45. K. Prasad, S. Bhagat, K. Amar Nath, S.N. Choudhary, K.L. Yadav, "Electrical conduction in $Ba(Bi_{0.5}Nb_{0.5})O_3$ ceramic: Impedance spectroscopy analysis", *Mater. Sci. Poland*, **28** [1] (2010) 317–325.
46. R. Maier, J.L. Chon, J.J. Neumeier, L.A. Bendersky, "Ferroelectricity and ferrimagnetism in iron-doped $BaTiO_3$", *Appl. Phys. Lett*., **78** (2001) 2536–2539.
47. B.A. Boukamp, "Electrochemical impedance spectroscopy in solid state ionics: recent advances", *Solid State Ionics*, **169** [1-4] (2004) 65–73.
48. G.D. Sharma, M. Roy, M.S. Roy, "Charge conduction mechanism and photovoltaic properties of 1,2-diazoamino diphenyl ethane (DDE) based Schottky device", *Mater. Sci. Eng. B*, **104** [1-2] (2003) 15–25.
49. M. Nadeem, M.J. Akhtar, A.Y. Khan, R. Shaheen, M.N. Haque, "AC study of 10% Fe-doped $La_{0.65}Ca_{0.35}MnO_3$ material by impedance spectroscopy", *Chem. Phys. Lett*.,

366 [3-4) (2002) 433–439.
50. K. Prasad, K.P. Chandra, S. Bhagat, S.N. Choudhary, A.R. Kulkarni, "Structural and electrical properties of lead-free perovskite $Ba(Al_{1/2}Nb_{1/2})O_3$", *J. Am. Ceram. Soc*., **93** [1] (2010) 190–197.
51. K. Prasad, K. Amar Nath, S. Bhagat, Priyanka, K.P. Chandra, A.R. Kulkarni, "Structural and electrical properties of lead-free ceramic: $Ba(La_{1/2}Nb_{1/2})O_3$", *Adv. Appl. Ceram.*, **109** [4] (2010) 225–233.
52. Y. Ishikawa, S. Akimoto, "Magnetic property and crystal chemistry of ilmenite ($MeTiO_3$) and hematite (αFe_2O_3) system II. magnetic property", *J. Phys. Soc. Jpn*., **13** [11] (1958) 1298–1310.
53. J.B. Goodenough, *Magnetism and the Chemical Bond*, John Wiley & Sons, New York/London, 1963, p. 183.
54. X. Deng, W. Lu, H. Wang, H. Wang, H. Huang, J. Dai, "Electronic, magnetic and dielectric properties of multiferroic $MnTiO_3$", *J. Mater. Res*., **27** (2012) 1421–1429.